Proton Film Packs for multi-shot experiments

Contact *Rob.Clarke@stfc.ac.uk*

Rob Clarke, Pete Brummitt, Steve Hook and Simon Spurdle,

Central Laser Facility, STFC Rutherford Appleton Laboratory

Harwell Oxford, OX11 0QX, UK

Introduction

The use of film packs is common-place as a spatial and energy diagnostic for proton beams. These beams are used as a direct diagnostic for the laser-plasma interaction, electron transport or as particle probe for other interactions. These packs typically contain Radiochromic film interspaced with energy filters, CR39 track detectors or foils for nuclear activation measurements. The multi-shot designs allow for several shots to be taken without the need to cycle the chambers between air and vacuum. This report outlines the new designs recently introduced and those already available.

Windmill design.

The original design for the proton film packs was that of a simple windmill (figure 1). Like all the designs described here, a lead filter shields the packs not in use from the on-shot radiation. The system automatically rotates to the next stack position, driven from a control box operated by the user. Each pack is individually removable and can operate with half or split-stacks.

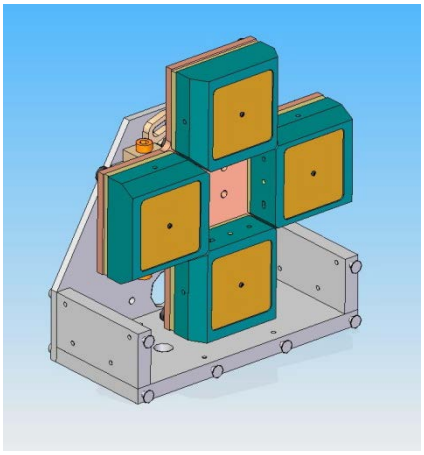

Figure 1. Windmill design

The windmill design has a large footprint, but minimizes the solid angle in the horizontal plane. When incorporating the shield at the front and mounting systems, the pack can operate at around 50mm from target.

Vertical Stack

The vertical stack design (figure 2) can be completely driven out of the way. It was originally designed to allow full beam diagnostics to be used either between or on alternate shots (such as OTR, focal plane monitors etc). The stack uses a single magazine which holds the 4 full stacks, half or split stacks. The main platform allows a second diagnostic to be attached which is driven in as the stacks are driven out.

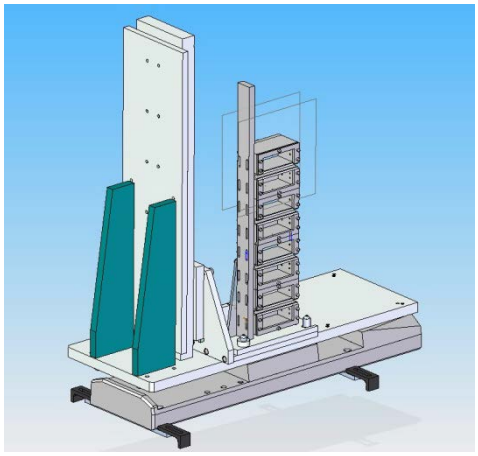

Figure 2. Vertical design

The design has a large footprint and is only driven manually (at present). The size restricts the distance from target at which it can be used to around 100mm.

Carousel Designs

The newest of the designs, the 3- and 5-position carousels (figures 3 and 4) are designed specifically to minimize the footprint in order to fit several film packs around the target in close proximity. Using the previous designs, using 2 or more packs restricts the target to pack distances to > 70mm, but with the new designs, distances < 50mm can be maintained.

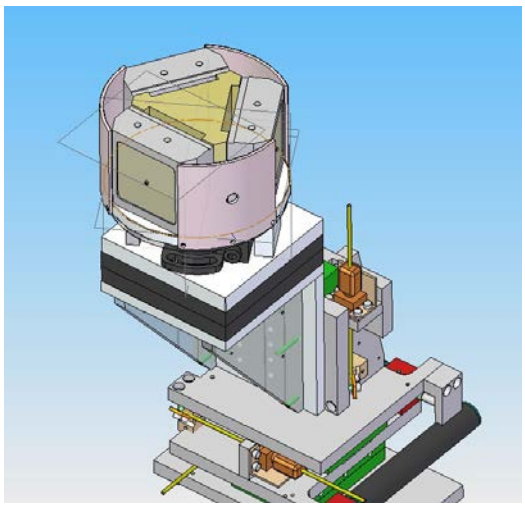

Figure 3. 3-position carousel design

The 3-stack design was initially designed to operate with a horizontal rotation, but the new 5-position version can also go out of plane. Both designs automatically reposition using the same controller as that for the original windmill design and can accept full or half stacks. A shield block in the centre provides shielding from one pack to the next, with a line of sight for other measurements (such as a magnetic spectrometer). Both

designs remove the entire carousel from the drive unit in order to quickly change packs.

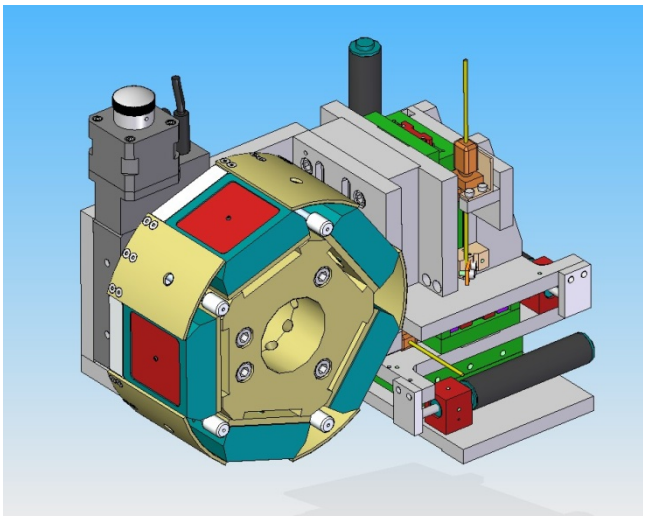

Figure 4. 5-position carousel design

Conclusions

The CLF in combination with visiting scientists has expanded the range of proton film pack designs in order to provide the most flexibility possible for experiments.

Acknowledgements

The CLF would like to acknowledge the many external user groups involved in the specification, design and subsequent development of these diagnostics.

Mitigation of EMP effects for imaging specularly reflected light on VULCAN PW

Contact:*ross.gray@strath.ac.uk*

R. J. Gray and P. McKenna
SUPA, Department of Physics, University of Strathclyde, Glasgow, G4 0NG, UK

N. Booth and D. Neely
Central Laser Facility, STFC Rutherford Appleton Laboratory, Didcot, Oxfordshire, OX11 0QX, UK

Intense laser-solid interactions produce a multitude of radiation. X-ray emission has been well described. Electron acceleration and emission is being studied in detail. Proton acceleration is a key area of research for future applications of laser-plasma interactions. Neutron emission has been researched in detail to better understand possible future applications of laser-plasma interactions in inertial confinement fusion. One area, however, is much less well understood and yet can have serious implications for the types of measurements that can be made in intense laser-plasma experiments.

The electromagnetic pulse (EMP) generated during the laser-plasma interaction is broadband and intense[1]. Electronics with close proximity to the interaction point are often disrupted. Computers often freeze and can even be seriously damaged. High voltage power supplies, for particle spectrometers for example, often overload and reset due to high voltage spikes generated by the interaction. Critically, CCD cameras are also affected by the EMP and often freeze. The EMP arrives at the CCD at the same time, if not before, the light from the interaction that is being imaged. This means the camera is disrupted by the EMP before the resulting data can be transfered to the data recorder or PC.

Finding suitable techniques to shield sensitive electronic equipment from EMP while still allowing free access for maintainence, allignment and development forms the basis of a problem which results in the underuse of diagnostic techniques that, while they may provide deep insights, are simply not practical to implement. Previous techniques to reduce the impact of EMP include, electronic filtering[2] or electrical isolation using a faraday cage.

In this short report we introduce an alternative technique for EMP mitigation, which is exclusively suited for optical systems containing sensitive electronic components. During a recent experiment on the Vulcan petawatt facility this diagnostic was used to image the specularly reflected laser light . A schematic is shown in Fig.2. A high magnification, Canon telephoto lens is used to image a scattering screen inside the interaction chamber from $\approx$ 4 m away. A large diameter fiber optic bundle was then used to direct the output of the lens to an optical table placed away from the line of sight of the interaction and behind minimal EMP sheilding.

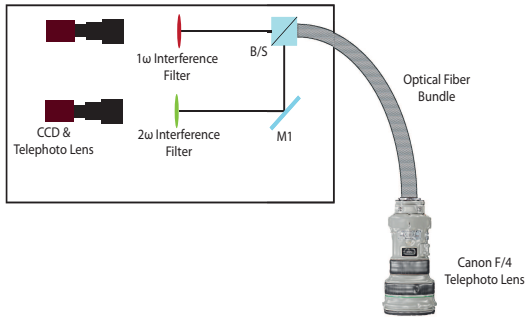

FIG. 1: Schematic of diagnostic arrangement. High magnification lens and fiber optic bundle provide standoff distance from interaction and allow access for multiple output channels.

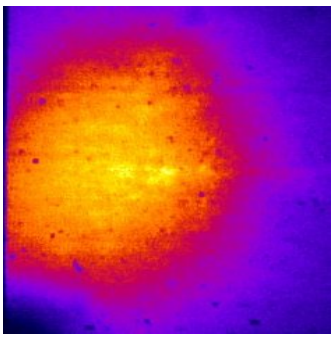

FIG. 2: Example image of specularly reflected light taken with fiber bundle arrangement.

The output from the fiber is then put through a 50/50 beam-splitter, splitting the light into two channels. One channel is filtered for the central laser wavelength and the second channel is filtered for the second harmonic of the laser wavelength. This enables a simultaneous measurement of the spatial-intensity profile of both the specularly reflected laser light and the laser light which is frequency doubled in the laser plasma interaction.

An example image of the output 1ω channel is shown in Fig.2(a). The resolution of the image is limited by the number of fibers in the bundle. While this is less than the number of pixels on the camera used, the resolution on the image produced is sufficiently high to enable the type of analysis described in previous reports[3].

Overall, the addition of a high magnification fiber coupled lens allows for a much larger standoff distance from the interaction point and enables the sensitive electronic equipment to be placed behind shielding and away from the interaction line of sight. Over the course of many full power laser shots, no effects due to EMP, either on the camera or computer, were observed.

[1]M. J. Mead *et al.*, Review of Scientific Instruments **75**, 4225 (2004).
[2]J. Lazarus *et al.*, Rutherford Appleton Laboratory- Central Laser Facility Annual Report (2004/05).
[3]R. J. Gray *et al.*, Rutherford Appleton Laboratory- Central Laser Facility Annual Report (2010/11).

Modified Thomson parabola design for high energy, multispecies ion sources

Contact *s.kar@qub.ac.uk*

D. Gwynne, S. Kar and M. Borghesi

Centre for Plasma Physics,
Queen's University Belfast
Belfast, BT7 1NN, UK

1. Introduction

High power lasers are nowadays able to accelerate protons and heavier ions up to tens of MeV per nucleon via various mechanisms such as target normal sheath acceleration (TNSA)[1], radiation pressure acceleration (RPA)[2] and break-out afterburner acceleration (BOA)[3]. Typically these mechanisms accelerate simultaneously several ion species, originated not only from the bulk target material, but also from the contaminant layers present on both side of the target foils due to poor vacuum conditions. Therefore, one would require discrimination between different charge species in order to obtain spectra of individual ion species, which is useful not only from a characterization point of view, but also to understand the underlying acceleration mechanisms. Among several routinely used ion diagnostics in such experiments, such as Radiochromic Film stack detectors, nuclear activation techniques, Faraday cups, Thomson Parabola Spectrometers (TPS) are particularly useful as different ion species are dispersed in energy and charge-to-mass ratio by means of static electric and magnetic fields[4-6]. Not only the diagnostic provides species resolved ion spectra, but also implementation and data analysis are relatively simple and straightforward.

Dispersion of ions in a TPS is governed by electric and magnetic field strengths as well as the dimensions of various elements, such as the field regions, distance from electric and magnetic fields to the detector etc. Currently used compact (in order to fit inside the vacuum interaction chamber) spectrometers are unable to provide sufficient charge state resolution beyond several MeV/nucleon heavy ions (as the parabolic ion traces starts to overlap), which limits the energy range of spectral measurements even when the energy dispersion by the magnetic field is adequate. Species separation can be increased primarily by increasing either the electric field strength or the extent of the electric field region. However, the large electric field required for separating high energy ion tracks will cause lower energy ions to be deflected away from the detector, or clipped by the electric plates itself. Hence the goal of obtaining a full energy spectrum is compromised. In this paper we discuss how shaping of the electric field plates for the TPS, can allow both low and high energy ions to be retained while providing significant species separation at the high energy end.

2. Theory and background

The schematic of a traditional TPS used in laser plasma experiments is shown in Figure 1. It consists of pairs of permanent rectangular magnets and electrodes, producing uniform magnetic and electric fields dispersing ions according to their charge-to-mass ratio and energy[4], producing a unique parabola on the detector plane for each charge species. The magnetic and electric fields are parallel to each other, but perpendicular to the ion's initial momentum. The pinhole selects the pencil beam of ions as input to the TPS. For a uniform electric and magnetic fields, without considering fringe field effects, the final (at the detector plane) deflections along Y (due to magnetic field) and X (due to electric field) axes for an ion with velocity $\mathbf{v_z}$, mass m and charge **q** can be derived respectively as:

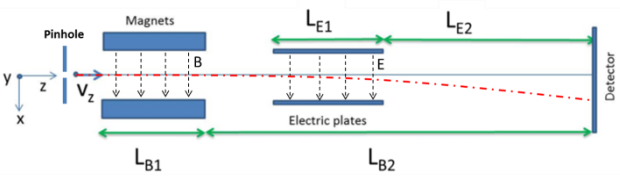

Figure 1: Schematic diagram of a TPS.

$$S_B = \frac{qBL_{B1}^2}{2mv_z} + \frac{qBL_{B1}L_{B2}}{mv_z}$$

Equation 1

$$S_E = \frac{qEL_{E1}^2}{2mv_z^2} + \frac{qEL_{E1}L_{E2}}{mv_z^2}$$

Equation 2

where $\mathbf{L_{B1}}$, $\mathbf{L_{B2}}$, $\mathbf{L_{E1}}$ and $\mathbf{L_{E2}}$ correspond to the distances shown in Figure 1, and, **E** and **B** denote the electric and magnetic field strengths respectively. The deflection due to the magnetic field ($\mathbf{S_B}$) is derived using equations of motion and Lorentz force, where one can neglect the change in $\mathbf{v_z}$ without any loss of generality.

Equations 1 and 2 show that the resulting deflections have a linear dependence on the magnetic and electric field strengths, whereas there is a stronger dependence on the length of either the magnets or the electric plates. In this paper we have focused on the electric field deflection, considering the energy dispersion produced by the magnetic field is adequate. For instance, in order to benchmark our calculations, we have considered a traditional TPS[4,5] consisting of 50 mm x 50 mm square magnets providing a peak magnetic field of 0.5 T. Other relevant parameters of this TPS are $\mathbf{L_{B2}}$=235 mm, $\mathbf{L_{E1}}$=50 mm and $\mathbf{L_{E2}}$=165 mm. The magnetic dispersion in this system is shown in Figure 2. It is to be noted that the magnetic field can be increased up to 1T if necessary, by using commercially available permanent magnets at 5 mm separation.

As mentioned earlier, in case of a multi species ion source, the electric field dispersion is equally important for resolving ion spectra. If the deflection due to the electric field is insufficient, it will be difficult to discriminate individual ion species due to overlapping of the parabolic traces towards the higher energy end, as observed in recent experiments using ultrathin foils carried out on the GEMINI and VULCAN facilities. In order to study a suitable field configuration for effective charge state separation, while retaining low energy ions, we used 3D particle tracing simulation PTRACE, as discussed below.

3. Simulation design

The particle tracing code PTRACE, written in C++ object oriented methodology[7], computes the trajectory of a particle through a customized 3D electromagnetic field region using a differential equation solver at its core. The numerical algorithm is a fourth order Runge-Kutta solver coupled with an adaptive step-size monitoring routine. The main advantage of such an approach is that it offers a fast and reliable solution to the

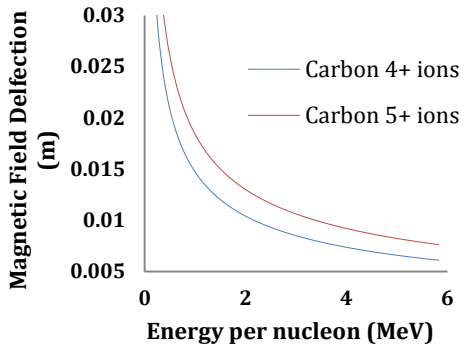

Figure 2: Deflection of ions by a standard TPS with a pair of 50x50 mm magnets producing a magnetic field of 0.5T.

equation of motion, with the possibility of prescribing the precision to which the trajectory is computed.

A 3D setup of the TPS was modeled in the PTRACE as per the schematic shown in the Figure 1. The pencil beam of ions, selected by the pinhole of the TPS, was defined in the PTRACE as a point ion source with multi-energy spectrum and very low divergence. The magnetic field region was defined next to the source. In order to include fringe fields, the magnetic field in this region was defined as per the field profile in a conventional magnet-yoke configuration, as measured by Carroll et. al[5]. Along the ion propagation axis (Z –axis), the field profile can be fitted with a super-Gaussian function

$$B(z) = B_{peak}\, exp\left[\left(\frac{z - z_{centre}}{B_{FWHM}/2}\right)^4\right]$$

Equation 3

where, $\mathbf{B_{peak}}$ is the peak magnetic field, $\mathbf{z_{centre}}$ the **z** coordinate of the center of the magnets and B_{FWHM} is the full width at half maximum of the field profile, which is approximately equal to the length of the magnets.

In order to study the effect of different charged plate geometries, we implemented a simple approach for electric field calculation. As shown in the Figure 3, the electric field at any given point in space **P(x,y,z)** is numerically calculated by superposition of the electric fields due to all points in the charged plates. For example, in the case of a rectangular geometry, the electric field $\vec{\mathbf{E}}$ owing to the positive electrode will therefore be:

$$\vec{E} = K\sigma \int_{y_{min}}^{y_{max}} \int_{z_{min}}^{z_{max}} \frac{dy'dz'\overrightarrow{P'P}}{\left|\overrightarrow{P'P}\right|^3}\Bigg|_{x'=x_p}$$

Equation 4

where $\mathbf{K=1/4\pi\varepsilon_0}$ and the surface charge density $\boldsymbol{\sigma=2\varepsilon_0 E}$. In order to simplify the calculation, the integration over **z** was substituted with a summation along **z**.

During the transit of an ion of given mass, charge and energy, the PTRACE main module accesses the electric and magnetic field objects in order to obtain the fields at its current position. The trajectory of the ion is subsequently simulated by the differential equation solver. The detector plane was defined at a given distance from the electric plates, which produces 2D images of the simulated parabolic ion traces.

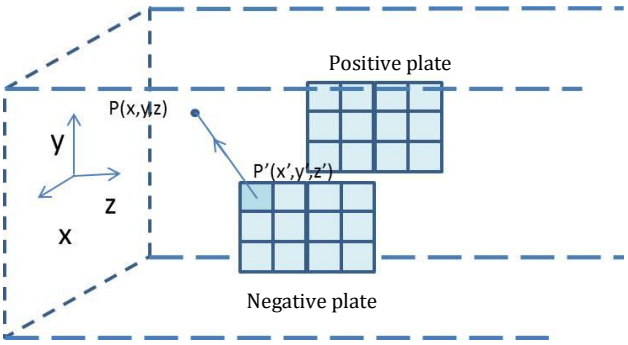

Figure 3: schematic of the electric plate setup in PTRACE for calculation of the E-field.

4. Increasing Species Separation

In principle, the species separation can be increased by three possible methods, such as increasing the distance $\mathbf{L_{E2}}$, increasing the electric field strength, and increasing $\mathbf{L_{E1}}$. Increasing $\mathbf{L_{E2}}$ is not a viable option as this merely increases the magnification of the data. Therefore the real resolution for discriminating the traces, which is defined by the pinhole size of TPS, remains unchanged. Moreover, there would be a decrease in the photon flux at the detector plane giving rise to lower signal to noise ratio.

The electric field strength can be increased either by decreasing the separation of the electrodes or by increasing the voltage to the electrodes. However, the limiting factor is the breakdown threshold at a given vacuum pressure. For example, up to ~ 20 KV/cm can be applied at a vacuum pressure of 10^{-4} mbar, avoiding any significant discharge flash that may cause increase in background level of a detector[6].

On the other hand, increasing the length of the electric plates is not limited by any fundamental constraints. Nevertheless, as can be seen from Equation 2, deflection due to electric field has a more effective dependence on $\mathbf{L_{E1}}$ than on the electric field strength **E**. One can write a simple scaling parameter, s_f, as the ratio between the deflection produced by $\mathbf{L_{E1}}$ long electric plates at field strength of **E** and $\mathbf{L'_{E1}}$ long electric plates at field strength of $\mathbf{E'}$

$$s_f = \frac{E'}{E}\,\frac{L'_{E1}}{L_{E1}}\left(\frac{L'_{E1} + 2L_{E2}}{L_{E1} + 2L_{E2}}\right)$$

Equation 4

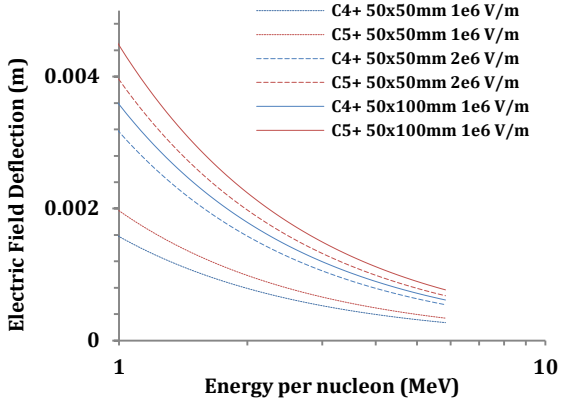

Figure 4: Comparison between electric field deflections produced by a 50x50mm plate and $1x10^6$ V/m (dotted lines), a 50x50mm plates at $2x10^6$ V/m (dashed lines), and, 50x100mm plates at $1x10^6$ V/m (solid lines).

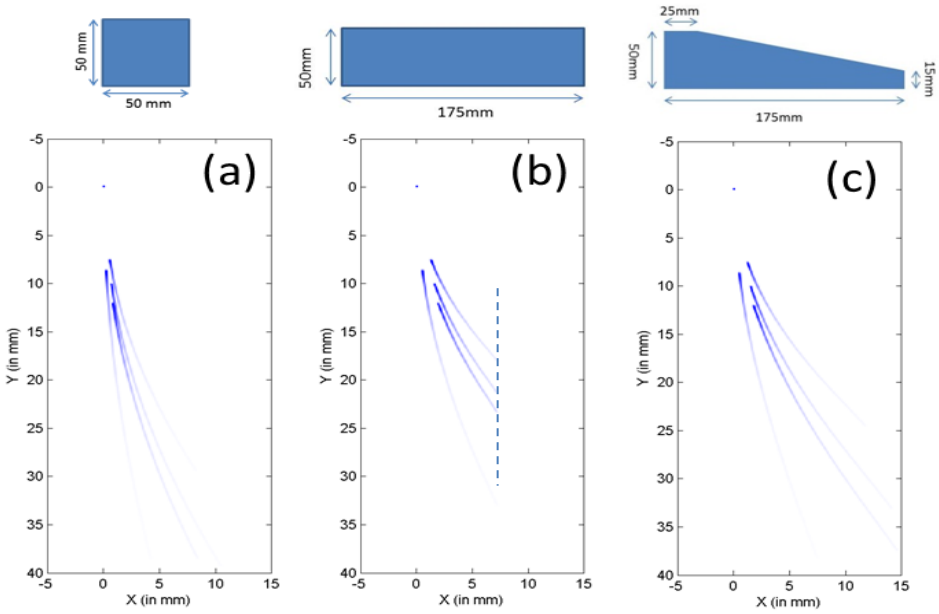

Figure 5: Comparison between the Thompson parabola traces for several ion species (proton, C^{6+}, C^{5+} and C^{4+} from left to right respectively) obtained using different electric plate designs – (a) 50 mm x 50 mm rectangular plates, (b) 50 mm x 175 mm rectangular plates and (c) 50 mm x 175 mm trapezoidal plate as shown on top of the simulated images. All other parameters were kept same in all cases, viz. E=1x10^6 V/m, B=0.5T, L_{B1}=50mm, L_{B2}=235 mm. The species separation is significantly improved by using longer electric plates at same potential. However, the low energy ions are clipped by the rectangular plate, as shown by the dotted line in (b). The trapezoidal plate allows the low energy ions to pass over the top of the plate, while keeping the same trace separation for high energy ions obtained in (b).

The reason behind the more effective dependence with the length of the electric plates is the increase in ion transit time inside the electric field region. Figure 4 shows a comparison between electric field deflections produced by different configurations, which illustrate the effectiveness of increasing the electric plate length over increasing the peak electric field.

In order to illustrate the effect of increasing electric plate length on charge state separation, we simulated the performance of TPS with PTRACE by changing the electric plate length, while keeping all other parameters identical as the standard TPS configuration (as mention in the section 2). One can see the dramatic improvement in separation between the traces of different charge state at high energy end for 175 mm long electric plates as shown in the Figure 5(b) as compared to the output of the standard TPS shown in the Fig. 5(a).

Using a longer electric field region instead of a higher electric field also provides flexibility in terms of controlling the deflection for different energy ions – by reshaping the geometry of the plates. As described earlier, it is important to retain the lower energy part of the ion spectrum. While using longer electric plates, the low energy ions hit the output end of the electric plates, which can be seen as a clipping in ion traces on the detector (as shown by the dotted line in the Figure 5(b)). Since the magnetic deflection, prior to the electric plates, disperses the ions along the vertical direction (y- axis) as per their energy, reshaping the plates into a trapezoidal geometry (for instance as shown in the Figure 5(c)) will allow the low energy ions to avoid clipping by the charged plates producing full ion spectrum as shown in the Figure 5(c). Since different energy ions are experiencing different lengths of electric field in a trapezoidal geometry, the output ion traces will not follow a perfect parabolic profile. However, as long as the ion traces are well separated and their charge states can be identified, the spectral profile can be obtained by deconvolving the traces after binning the signal along the Y axis, i.e. along the axis of the energy dispersion caused by the magnetic field.

6. Conclusions

With the growing need for a compact, high resolution ion spectrometer for 10s MeV/nucleon ions, produced by high power laser plasma interaction, we have studied a potential modification to the standard Thompson parabola spectrometer currently used in experiments. We have proposed to use an extended, trapezoidal shaped electric plates, which will provide not only better trace separation for high energy ions (due to the extended length of the electric plates), but also will retain the lower energy part of the spectrum. The latter will be achieved by using a trapezoidal shape, instead of rectangular shape, for the electric plates as it allows the low energy ions to reach the detector, which could otherwise have been clipped by the electric plates.

References

1. M. Borghesi et al., Fusion Sci. Tech. **49**, 412 (2006). J. Fuchs et al., Nat. Phys. **2**, 48 (2006); L. Robson et al., Nat. Phys. **3**, 58 (2007); M. Passoni et al., New J. Phys. **12**, 045012 (2010).
2. T. Esirkepov et al., Phys. Rev. Lett. **92,** 175003 (2004); S. Kar et al., Phys. Rev. Lett. **100**, 225004 (2008); A.P.L. Robinson et al., Plasma Phys. Control. Fusion, **51**, 024004 (2009); A. P. L. Robinson et al., New J. Phys., **10**, 013021 (2008); A. Macchi et al., New J. Phys. **12**, 045013 (2010); B.Qiao et al., Phys. Rev. Lett., **108**, 115002 (2012); S. Kar et. al., arXiv:1207.4288v1 [physics.plasm-ph]
3. L. Yin et. al., Phys. Rev. Letts., **107**, 045003 (2011); D. Jung et. al., Phys. Rev. Letts., **107**, 115002, 2011
4. M. Rhee et al. Rev Sci. Inst. **58** 240 (1987); S. Sakabe et. al., Rev. Sci Inst. **51**, 1314-1315 (1980).
5. D. Carroll et al., Nucl. Inst Meth. Phys. Res. A **20** 23-27 (2010); K. Harres et al., Rev. Sci Inst., **79** 093306 (2008); J. Morrison et al. Rev. Sci Inst. **82** 033506 (2011).
6. D. Jung et al., Rev. Sci Inst. **82** 013306 (2011).
7. A. Schiavi. PhD thesis, Imperial College London (2003).

Cryogenic pump induced vibration in the TAP Interaction Chamber

Contact *steve.blake@stfc.ac.uk*

Steve Blake, Philip Hackett, Rob Clarke, Alistair Cox

Central Laser Facility, STFC, Rutherford Appleton Laboratory, HSIC, Didcot, Oxfordshire, OX11 0QX, UK

Introduction

The SHI Marathon CP-16 Cryogenic vacuum pump has been installed on both the TAP and Gemini Interaction Chambers. It has consistently delivered an improvement in vacuum levels by one decade instantly. Cryogenic vacuum pumps are a source of vibration and this has impacted experiments in Gemini. Due to the problems on Gemini an investigation was instigated to determine the effect on TAP and improve our knowledge of good chamber design. This report details the use of a number of analysis techniques to determine whether the Cryogenic pump could be directly connected to the TAP interaction chamber without impeding experiments.

The Cryopump contains a displacer, acting with a constant-frequency reciprocating motion along the axis of the pump, and is rigidly attached to the chamber wall by a bolted flange (Figure 1). This mechanical vibration input to the chamber operates at approximately 2Hz.

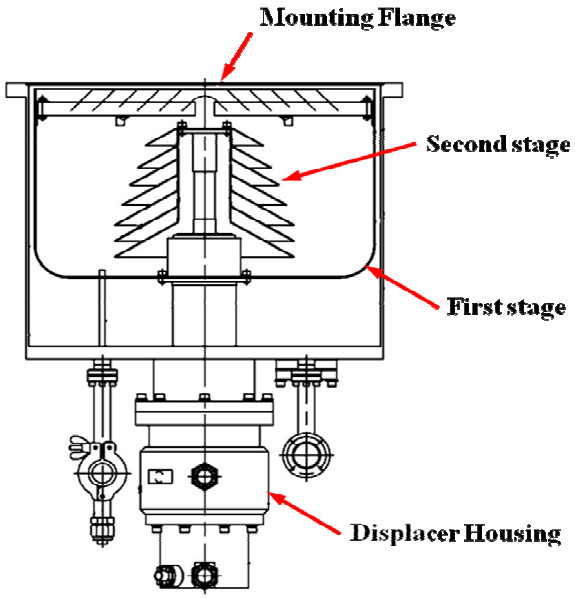

Figure 1: Cross-section of SHI CP-16 Cryopump

An initial test on TAP suggested that the Cryopump vibration did not affect the focusing optics or target. It was presumed that the mass of the chamber and its coupling with the concrete plinth provided sufficient mass to overcome any vibration caused by the reciprocating displacer. In order to confirm the initial findings a three-pronged investigation was carried out utilising motion transducers and beam pointing diagnostics. The stages of investigation were:

1. Measurement of vibration accelerations in the target chamber structures plotting the acceleration spectrum across a frequency range of 0-125Hz.
2. Measurement of the vibration velocities on the target chamber structure and the Cryopump, to determine point displacements at peaks in the frequency spectrum found in the first test.
3. Measurement of beam pointing stability

Test equipment

To measure vibration at points in the chamber and on the Cryopump, the Data Physics data acquisition system, a set of three ICP seismic accelerometers and a pair of piezoelectric velocity transducers were used.

Data Acquisition System

The DP SignalCalc ACE portable Dynamic Signal Analyser (DSP) consists of a 4-channel USB-powered 'Quattro' DSP unit with a 24-bit ADC and integral anti-aliasing filter dedicated to each input, and a PC-based interface and data display in the form of the SignalCalc software application. The specification of the DSP is shown in Table 1 and an image in Figure 2. The DSP performs all signal processing and the software application is used to control tests, generate plots and record throughput data for later analysis and post-processing. The signal processing power and high sample rate allows for a high measurement resolution and accurate results, in conjunction with the low-frequency range and high sensitivity of the accelerometers.

Averaged data taken in fixed length 'frames' of sampling from the sensor signals gives a time-domain result which may be transformed to the frequency domain using the FFT algorithm. Graphs can be generated which show a spectrum of levels of the quantity measured (acceleration or velocity) across a frequency range set at the beginning of the test. The simultaneously recorded throughput data is a non-averaged time history of the sensor signals during the test which can be re-sampled by the DSP at any point after the test, as if in real time. Specific time windows can also be selected if required. Using these tools the analysed data was selected carefully to avoid general daytime site noise and staff noise. Many tests were carried out overnight or at weekends.

Table 1 DSP system specifications

Model	Data Physics SignalCalc Ace
Channels	4 (input)
Sample rate (each ch)	204.8 kHz
Signal processing (each ch)	32-bit DSP, 24-bit ADC
Dynamic range	120dB
Measurement resolution	25,600 lines

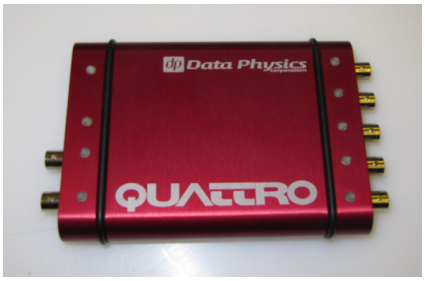

Figure 2: An image of the Quattro DSP

Sensors - acceleration

The ICP accelerometers shown in Figure 3 with the specification in Table 2 are small self-contained units which condition their own signal and are directly connected to the DSP input. The calibration information is shown in Table 3. Seismic types have a low range of acceleration measurement but a consequently high sensitivity, making them suitable for measuring ultra-low levels of vibration and low frequencies. They are likely to be damaged by high-energy sources and cannot be used to measure input vibrations directly from such sources.

Table 2 ICP seismic accelerometer specifications [1]

PCB 393B05 ICP accelerometer	
Sensitivity (± 10 %)	10 V/g
Measurement Range	0.5 g peak
Frequency Range (± 5 %)	0.7 to 450 Hz
Frequency Range (± 10 %)	0.5 to 750 Hz
Frequency Range (± 3 dB)	0.2 to 1700 Hz
Resonant Frequency	≥ 2.5 kHz
Broadband Resolution (1 to 10,000 Hz)	0.000004g rms
Non-Linearity	≤ 1 %
Transverse Sensitivity	≤ 5 %

Table 3 Accelerometer calibration data

Serial No.	**Sensitivity**	**Calibration date**
16017	9.76 V/g	02.09.2010
29913	10.09 V/g	08.11.2010
29914	10.35 V/g	08.11.2010

Figure 3: ICP® High-Sensitivity Accelerometer [2]

Sensors - velocity

To measure the vibration spectrum on the Cryopump when running, and local points in the chamber, a pair of velocity transducers were used. These are shown in Figure 4. These have a larger range of measurement suitable for measuring close to sources. Low-frequency measurement to a given accuracy is 4Hz minimum.

Table 4 Velocity transducer specifications

SinoCeramics CS-YD-00X	
Linear Range	2000 mm/s
Frequency Range	4Hz to 4kHz
Temp Range (degC)	-10 to +70
Output	±5V

Figure 4: SinoCeramics Velocity Transducer [3]

Test Specification

Input measurement

It is desirable in determining the vibration response of structures to measure the known input vibration sources, as closely as possible to their interface with the structure under test to avoid measuring modal behaviour or resonance in intermediate structures.

In the case of the Cryopump the casing which houses the displacer, the flange attachment to the chamber wall and the chamber wall itself are all reasonable points to take an input measurement. The high-sensitivity seismic accelerometers used for the initial test could not be placed on the pump casing due to their low g-range of operation. The lack of mounting points on the chamber wall also led to the use of a platform and bracket mounting being used for a seismic accelerometer inside the chamber (Figure 5). This measurement can be considered more as an indicator of response in the chamber itself, close to the source. The accelerometer was orientated to correspond with the displacer axis (along the North-South axis of the chamber). A pair of more robust velocity transducers was used on the pump casing in the second test to determine an input spectrum.

Response measurement

A period during which there were minimal disturbances other than the Cryopump was used for testing, although the vibration spectrum in the chamber still reflects a broadband random input. All data was taken with the chamber under vacuum.

Acceleration testing

Response measurement in chamber – seismic accelerometers

For the initial test, three seismic accelerometers were placed in the chamber to measure response (Figure 5):

- On a platform fixed to the North end inside wall
- On the parabola mirror frame in the horizontal plane, along the chamber North-South axis
- On the breadboard vertical axis.

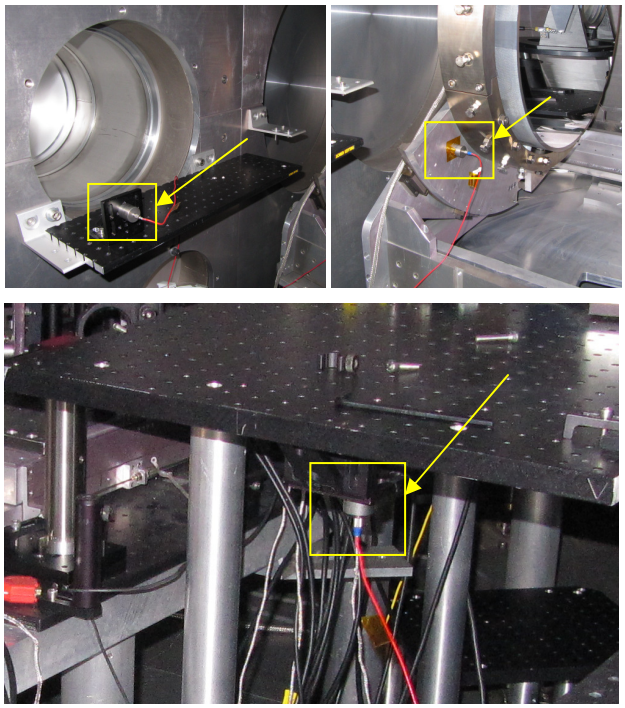

Figure 5, Clockwise from top left: chamber North end, parabola frame, breadboard

Recorded data

Acceleration time history was recorded from the 3 accelerometers, over 3 days. Analysis was conducted on sections of the data 11.5 hrs in length.

Measured response spectra

Below are the spectra from 0-125Hz of acceleration in g, with the Cryopump running and switched off, for each point.

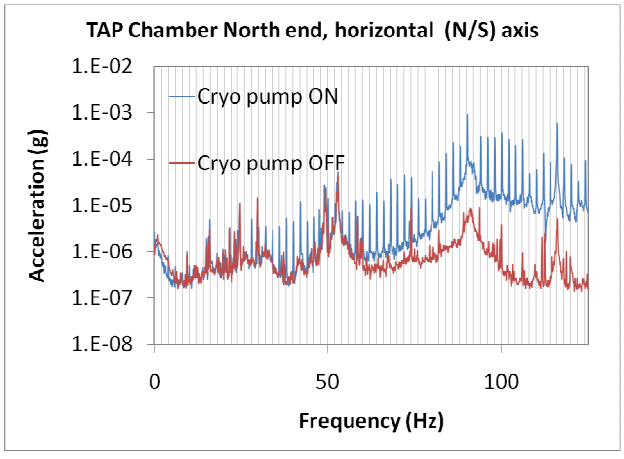

Figure 6: 0-125Hz acceleration spectrum at chamber N end

It can be seen in Figure 6 above that there is a set of peak responses at intervals of 2Hz, which are at multiples of 2Hz, and that the levels increase with frequency (Figure 7, below).

For a given level of acceleration however, the resulting displacement will be lower at higher frequencies, so that a higher level of acceleration at higher frequency does not necessarily mean a larger displacement. The peaks are not present with the pump switched off.

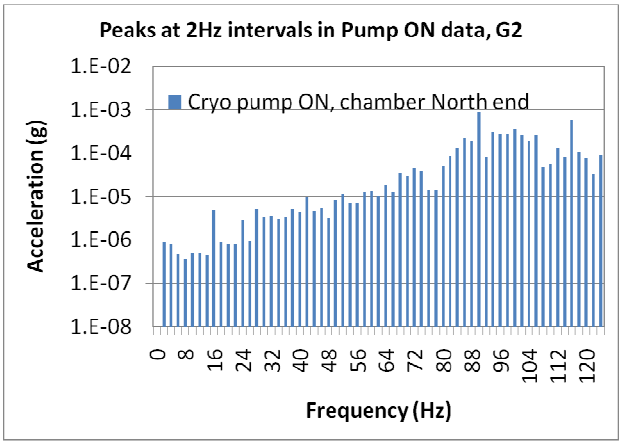

Figure 7: Peaks at 2Hz intervals across acceleration spectrum at chamber North end, with Cryopump running

The response of the parabola frame (Figure 8, below) shows that the 2Hz-multiple peaks are only visible above about 60Hz, and they are at a significantly lower level than peaks at 15.5Hz and 24.5Hz, which exist with the pump switched off.

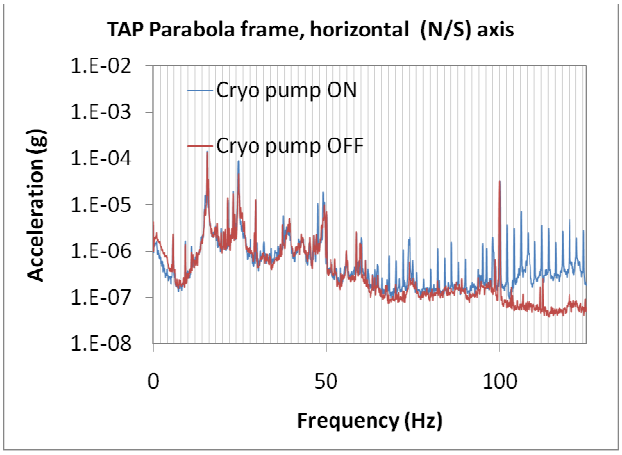

Figure 8: 0-125Hz acceleration spectrum at parabola frame

At the breadboard (Figure 9, below) the response at 2Hz-multiples is only visible above about 80Hz, again at lower levels than existing sources. The intensity at both parabola and breadboard is between approximately 1/10th and 1/1000th of that at the chamber North end.

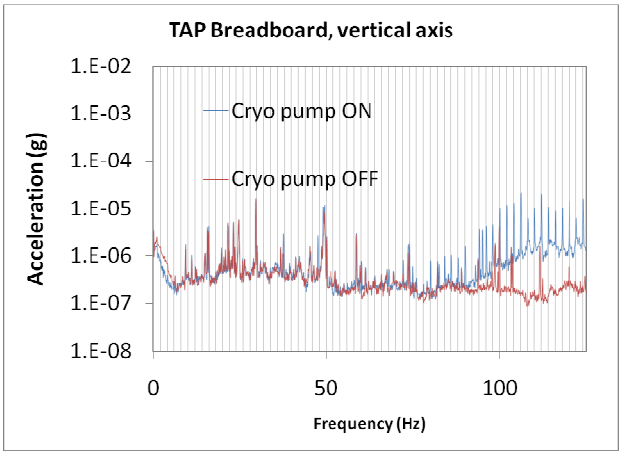

Figure 9: 0-125Hz acceleration spectrum at breadboard

Measured values of g do not give an insight into displacement values at the measured points. These can be gained by performing an integration operation on velocity measurements, which can be done automatically by the software.

Displacement testing

Source measurement of Cryopump – velocity transducers

In a second test, two velocity transducers were fixed to the Cryopump casing with epoxy resin to measure the spectrum of the pump vibration.

One sensor was fixed to the flat surface at the back of the pump casing, in line with the horizontal displacer motion. The second sensor was fixed to the cylindrical top surface of the casing along a vertical axis (Figure 10).

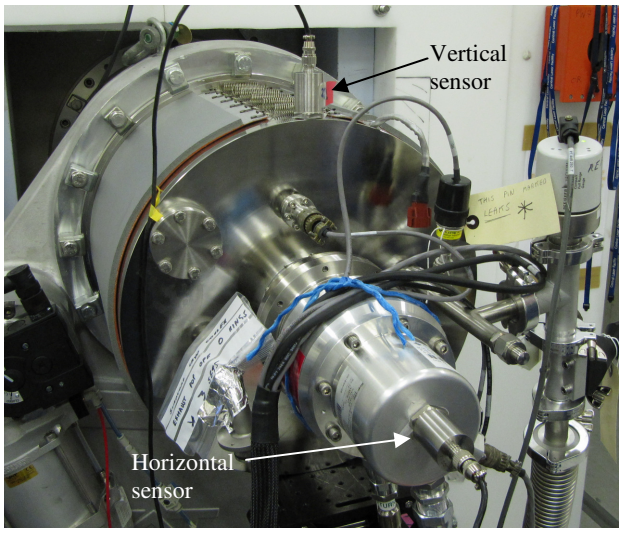

Figure 10: Input measurement sensor positions

Response measurement in chamber – velocity transducers

Sensors were placed at a point on each breadboard in the chamber, on the vertical axis. The parameter of interest at the measured points is displacement, which is derived from velocity measurements.

Recorded data

Velocity time histories were recorded from the Cryopump casing and from the breadboard over a period of around 1 hour. Analysis was conducted on the full length of recorded data minus the initial disturbed periods of set-up.

Post-processing

The SignalCalc software uses the Engineering Unit (EU) System whereby SI units of measurement are applied to the signal according to the sensor calibrated sensitivity values, i.e. 20.4VmV/EU for a velocity transducer, where the EU selected is mm/sec.

These SI units are expressed in terms of their dimensions of length and time, which for mm/sec are $L^1\ T^{-1}$. Where only the time exponent differs between EU, as between mm/sec and mm ($L^1\ T^0$) or between mm/sec and mm/sec^2 ($L^1\ T^{-2}$), the software can differentiate or integrate the signal with respect to time to yield a new measurement.

To derive displacement spectra from those of velocity, units of length (in mm) are selected on the vertical axis of the frequency-domain transform plot of G(xx), the Average Auto Power Spectrum, which by default is measured in mm/sec for velocity sensor signals. The values were exported from SignalCalc to Excel for re-plotting (Figure 11 below).

Measured input spectrum

Below is the spectrum of displacement from 0-125Hz as measured at the pump casing, in the horizontal (chamber N-S) and vertical axes.

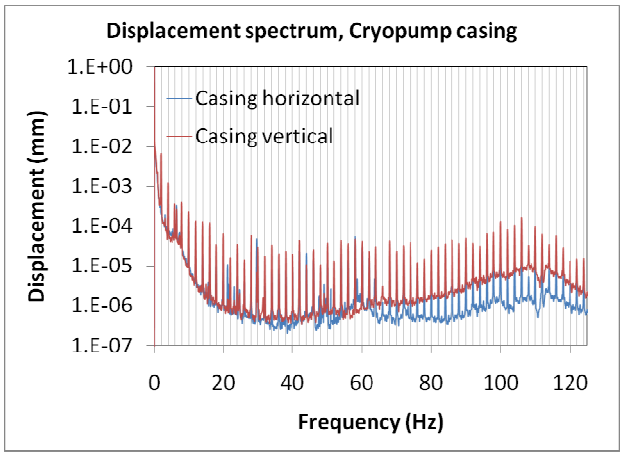

Figure 11: 0-125Hz displacement spectrum at Cryopump casing

In Figure 11 the 2Hz-multiple peaks, which are assumed to be harmonics of a fundamental frequency at 2Hz, can be seen clearly throughout the spectrum, and although the velocity transducers are rated only to 4Hz as a lower range of accurate measurement there are clear peaks at 2Hz and 4Hz rising out of the noise. The vertical vibration is somewhat stronger than the horizontal. It seems likely that the Cryopump displacer is the source, and that it is causing the responses seen in the seismic accelerometer data from the chamber.

Measured response spectra

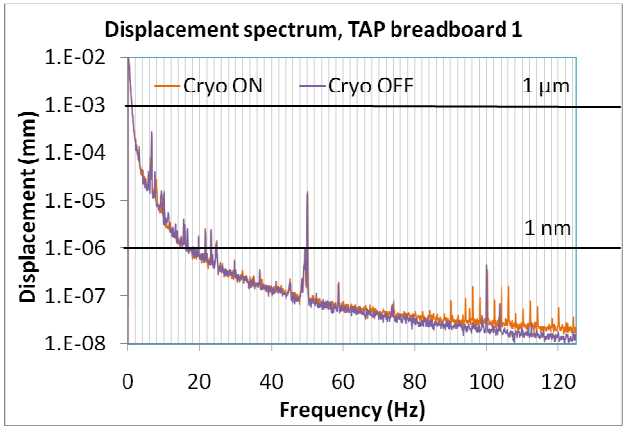

Figure 12: 0-125Hz displacement spectrum at breadboard 1

It can be seen from Figure 12 above that the displacements caused by the pump vibration are insignificant; occurring as they do at high frequency, and that the difference with the pump switched off is negligible below 80Hz.

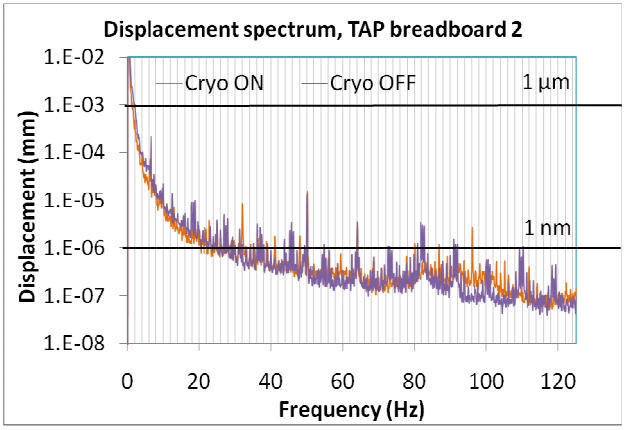

Figure 13: 0-125Hz displacement spectrum at breadboard 2

Figure 13 shows a plot of the second breadboard which appears to show higher levels across the spectrum but the displacements caused by the pump are still insignificant, with the worst at 32Hz being around 7nm.

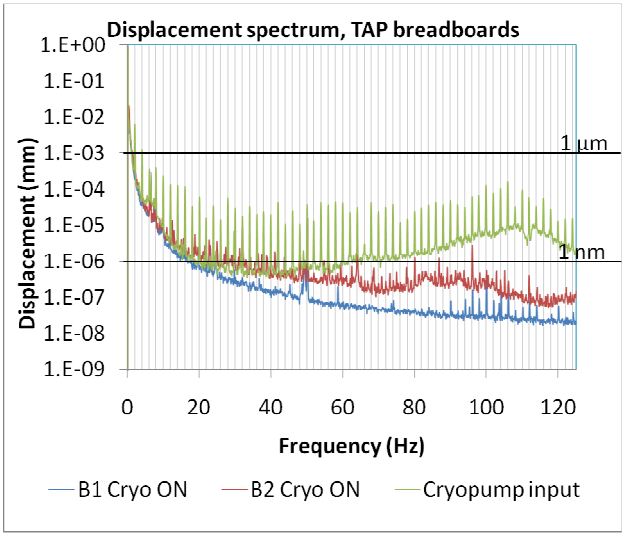

Figure 14: 0-125Hz displacement spectrum

Figure 14 is a comparative plot showing the breadboard displacement levels against the Cryopump vertical axis measurement. There is little coherence between the input and response signals and overall levels are significantly lower in the breadboards.

Recording of beam pointing stability

The final test was to propagate the alignment beam from LA4 through to the target location focussing the beam onto a camera which recorded an image of the spot. This recording was started then the Cryopump started and run for a time; the Cryopump was stopped and then at a time later the recording was stopped. A copy of the recording is included in this report. From the recording it was not possible to clearly identify when the pump was started or stopped.

Conclusions

The data shows that with the Cryopump directly connected to the TAP chamber the induced vibration on the breadboards and optical mounts is measurable, but insignificant. Work is on-going to see the Cryopump installed as a permanent feature on TAP available to visiting groups. A further Annual Report article will follow showing in more detail the benefit the Cryopump has on vacuum pumping speed and overall vacuum performance.

References

1. PCB. *ACCELEROMETER, ICP®, SEISMIC.* Revision H, ECN#: 29253. PCB Piezoelectronics Vibration Division, Depew, NY 14043, USA, 2008.
2. http://www.pcb.com/spec_sheet.asp?model=393B05&item_id=10938#photo
3. http://sinocera.com/vibration%20instrumentation-velocity%20and%20disp.htm

Acknowledgements

Much of this analysis was carried out by Phil Hackett during his short placement. Rob Clarke setup and captured the spot data showing the beam pointing stability. SHI Cryogenics provided the cutaway view of the Cryopump for inclusion in the report.